American Mineralogist, Volume 74, pages 1113–1123, 1989

High-resolution electron microscopy of stacking irregularities in chlorites from the central Pyrenees

ANTON-JAN BONS*
Department of Geology, Institute of Earth Sciences, University of Utrecht, P.O. Box 80.021, 3508 TA Utrecht, The Netherlands
DOMINIQUE SCHRYVERS
Centre for High-Voltage Electron Microscopy, University of Antwerp (R.U.C.A.), Groenenborgerlaan 171, 2020 Antwerp, Belgium

ABSTRACT

Fe-rich chlorites from slates from the Central Pyrenees (Spain) have been studied by high-resolution transmission electron microscopy (HRTEM) in combination with image calculations. These chlorites show various crystal imperfections, such as semirandom stacking and variations in lattice spacing. The semirandom stacking, which is common to most chlorites, is caused by shifts of magnitude $b/3$ parallel to the basal planes. The HRTEM images show that these shifts occur both in the 2:1 layer and at the level of the brucite interlayer. Local deviations of the (001) lattice spacing of 14-Å chlorite are caused by a local absence of the brucite interlayer (resulting in a lattice spacing of 9 Å) or by layers with a 1:1 phyllosilicate structure (lattice spacing 7 Å). The consequences of these observations for the study of deformation-induced defects in chlorite are discussed.

INTRODUCTION

Chlorite is a phyllosilicate that consists of alternating talc-like layers, with a general composition $(Mg,Fe,Al)_3(Si,Al)_4O_{10}(OH)_2$, and brucite-like layers, $(Fe,Mg,Al)_3(OH)_6$. It is an important rock-forming mineral in sedimentary rocks, low-grade metamorphic rocks, and igneous rocks (e.g., Bailey, 1988). Most chlorite crystals show structural disorder, resulting from rotations and shifts of successive layers and from intercalations of layers with a different structure or composition. This structural disorder has been studied with X-ray diffraction techniques, which only give information about the average crystal structure (e.g., Brown and Bailey, 1962; Shirozu and Bailey, 1965). More recently it has been demonstrated that high-resolution transmission electron microscopy (HRTEM) is useful in distinguishing individual shifts between successive layers (Veblen, 1983; Spinnler et al., 1984) and intercalations with a different structure (Veblen, 1983; Olives and Amouric, 1984; Maresh et al., 1985; Olives, 1985; Amouric et al., 1988).

This paper reports the results of a HRTEM study of chlorite crystals in slates from the Cambro-Ordovician Seo Formation of the Orri dome, central Pyrenees, Spain (Hartevelt, 1970; Speksnijder, 1987; Bons, 1988a, 1988b). The slates consist mainly of chlorite and muscovite, with minor amounts of quartz and albite. Grain sizes vary from a few micrometers up to 100 μm. Electron microprobe analyses indicate that the average composition of the chlorites is $Mg_{1.5}Fe_{2.8}Al_{1.7}[(Si_{2.6}Al_{1.4})O_{10}/(OH)_2](OH)_6$. Many of the chlorites have been deformed during slaty cleavage development (Bons, 1988a).

Conventional electron microscopy, using a JEOL JEM-200C transmission electron microscope at the University of Utrecht, has shown that these chlorites exhibit extensive stacking disorder and a high density of planar defects parallel to the chlorite layers (Bons, 1988a). Some of the planar defects in deformed grains occur in between dislocations and can be interpreted as deformation-induced stacking faults (Bons, 1988a). Other defects, invariably associated with deviating fringe spacings in lattice-fringe images and usually extending all through the crystal, occur in deformed and undeformed grains alike, as does the stacking disorder. It is most likely that they originated during crystal growth, although the 7-Å fringes described below may also have been formed during weathering, as they occur preferentially near grain boundaries. For detailed studies on the deformation mechanisms of chlorite (Bons, 1988a), it is necessary to know the nature of the stacking disorder and of the planar defects.

The stacking disorder is visible in electron-diffraction patterns as a streaking of rows of reflections with $k \neq 3n$. The planar defects characterized by a variation in fringe spacing show spacings of ca. 7 Å and 9 Å, instead of the 14-Å spacing of the chlorite (001) planes (Fig. 1). Such deviating lattice-fringe spacings can be caused by actual variations in lattice-plane spacing (Lee and Peacor, 1983; Veblen, 1983; Lee et al., 1984; Maresh et al., 1985; Ahn and Peacor, 1985; Amouric et al., 1988), but also by stacking faults (e.g., Fig. 7 in Amelinckx and Van Landuyt, 1976) or by variations in specimen thickness and orientation or electron-optical conditions (Jahren, 1988). In general the nature of planar defects can be analyzed

* Present address: Laboratory for Materials Science, Delft University of Technology, Rotterdamseweg 137, 2628 AL Delft, The Netherlands.

0003–004X/89/0910–1113$02.00

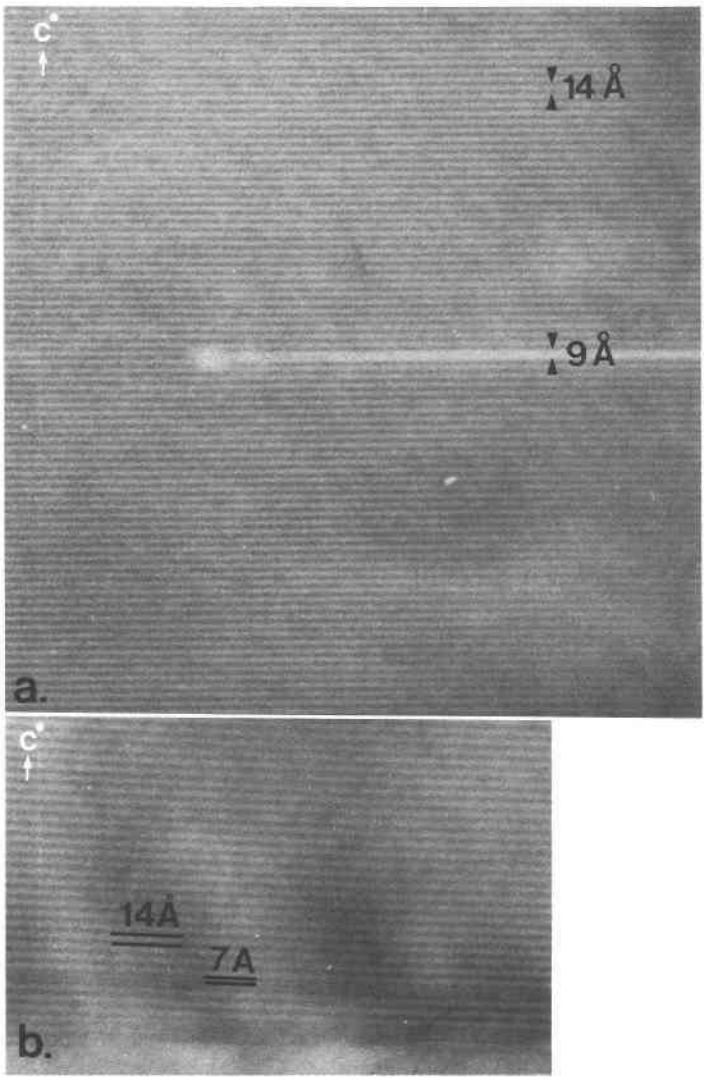

Fig. 1. Deviating fringe spacings in (001) lattice-fringe images of chlorites: 9-Å fringe (**a**) and 7-Å fringes (**b**) between 14-Å chlorite (001) fringes.

with conventional TEM using diffraction contrast (e.g., Edington, 1975). In order to do this analysis, the planar defects should be inclined to the electron beam. However, in the present case, defects inclined to the beam often overlap because of the high defect density. The overlap of defects, in combination with the stacking disorder, leads to a complex fringe contrast that hampers the determination of the nature of the defects (Bons, 1988a). When the planar defects are imaged edge-on, i.e., without overlapping, conventional TEM images do not yield useful information. Lattice images obtained with HRTEM do give structural information if the planar defects are viewed edge-on, provided the crystal is viewed along a major zone axis, e.g., along the [100] direction to study defects parallel to (001).

The instrument used in this study is a JEOL JEM-200CX transmission electron microscope fitted with a top-entry high-resolution pole piece; this instrument is located at the Centre for High-Voltage Electron Microscopy of the University of Antwerp (R.U.C.A.). The TEM specimens were prepared by fixing selected areas from standard petrological thin sections to Cu support grids, which are then thinned down to perforation by ion-beam milling.

Crystal structure

The basic structure of all phyllosilicates is a sheet of $(Si,Al)O_4$ tetrahedra linked together in a pseudohexagonal pattern (the tetrahedral sheet or T sheet), in which the **a** and **b** axes lie (Fig. 2a). In the group of 2:1 phyllosilicates, to which chlorite belongs, two of these tetrahedral sheets are sandwiched together to form a sheet of octahedral sites in between (the octahedral sheet or O sheet). The

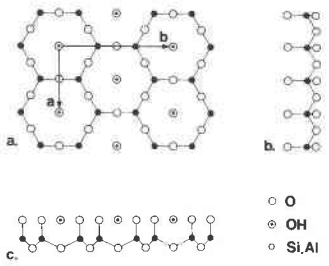

Fig. 2. The tetrahedral sheet of the crystal structure of the phyllosilicates. (**a**) Plan view of the tetrahedral sheet; the crystal axes **a** and **b** are indicated; the oxygens directly above the (Si, Al) positions have been omitted for clarity. (**b**) Projection of the tetrahedral sheet parallel to [010]. (**c**) Projection of the tetrahedral sheet parallel to [100]. In this projection the tetrahedra are concentrated in columns that are two tetrahedra wide, the *tetrahedral columns.*

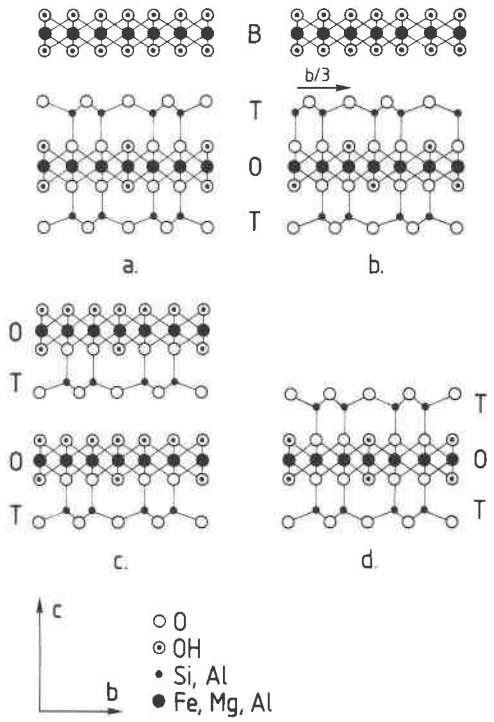

Fig. 3. Schematic representation of the crystal structure of chlorite and related phyllosilicates, projected parallel to [100]. T = tetrahedral sheet, O = octahedral sheet, B = brucite interlayer. (**a**) Chlorite; total thickness of one unit layer is 14 Å. (**b**) Chlorite with a shift of $b/3$ in the octahedral sheet of the 2:1 layer. (**c**) 1:1 phyllosilicate; two layers of 7 Å are drawn. (**d**) Talc structure; unit layer thickness is 9 Å.

octahedral sites can be occupied by various metal ions. This packet of tetrahedral-octahedral-tetrahedral sheets is often called the "talc" layer or T–O–T layer, although the term "2:1 layer" is preferable (Bailey, 1980a). The 2:1 layers are stacked in the direction of the **c** axis with or without interlayers.

Because of the pseudohexagonal symmetry of each sheet, every direction in the (001) plane has more or less equivalent directions at 60° intervals. For example, the pseudo-equivalent directions for [100] are [110] and [1$\bar{1}$0], and the pseudo-equivalent directions for [010] are [310] and [3$\bar{1}$0]. These pseudo-equivalent directions cannot be distinguished in practical TEM, and therefore the directions [100], [110], and [1$\bar{1}$0] will henceforward be indicated with ⟨100⟩; and [010], [310], and [3$\bar{1}$0] with ⟨010⟩. When the tetrahedral sheet is projected along the ⟨100⟩ directions, the tetrahedra are grouped to form "columns" with a width of two tetrahedra (Fig. 2c). These "columns" will henceforward be called *tetrahedral columns.* Projections parallel to ⟨010⟩ directions do not show such tetrahedral columns (Fig. 2b).

In talc the 2:1 layers are electrostatically neutral, and they are stacked in the direction of the **c** axis without any intervening layers (Fig. 3d). The chlorite structure consists of alternating 2:1 layers and brucite-like magnesium-iron-aluminum hydroxide interlayers. A single chlorite unit is formed by one 2:1 layer and one brucite interlayer; the total thickness is about 14 Å (Fig. 3a). Brown and Bailey (1962) determined that four different structural units, consisting of four different relative arrangements of 2:1 layers and interlayers, are theoretically possible. These structural units can be stacked in various ways, leading to a large number of regular one-layer polytypes (see Brown and Bailey, 1962; Bailey, 1980b; and Spinnler et al., 1984). However, many chlorites have irregular stacking sequences. In diffraction patterns they show sharp $k = 3n$ reflections and streaking of the $k \neq 3n$ reflections, indicating that the layers are related to one another by shifts of magnitude $b/3$ parallel to the sheets (Fig. 3b); this is termed semirandom stacking (Brown and Bailey, 1962; Bailey, 1988, 1980b; Brindley, 1980). The shifts can occur both at the level of the interlayer and within the 2:1 layer (Spinnler et al., 1984; this study). Most ordered chlorites in nature have a triclinic or monoclinic symmetry (e.g., Brown and Bailey, 1962; Bailey, 1988); the symmetry of the semirandom stacking sequences will usually be triclinic (Bailey, 1980b, 1988).

The 1:1 phyllosilicates are characterized by a single tetrahedral sheet attached to a single octahedral sheet (Fig. 3c). The basal spacing of the 1:1 phyllosilicates is ca. 7 Å (Bailey, 1980b).

Computer simulations

The interpretation of HRTEM images is not always straightforward. In the ideal case the image contrast of a very thin specimen at optimum (Scherzer) defocus represents the projected potential of the crystal, and a direct interpretation in terms of the crystal structure is possible (e.g., Van Dyck, 1986). However, in the majority of cases, HRTEM images should be interpreted by comparison with computer-simulated images, calculated using an assumed crystal structure as input and taking into account the experimental conditions of the microscope. In general some parameters will be known (e.g., spherical aberration, beam

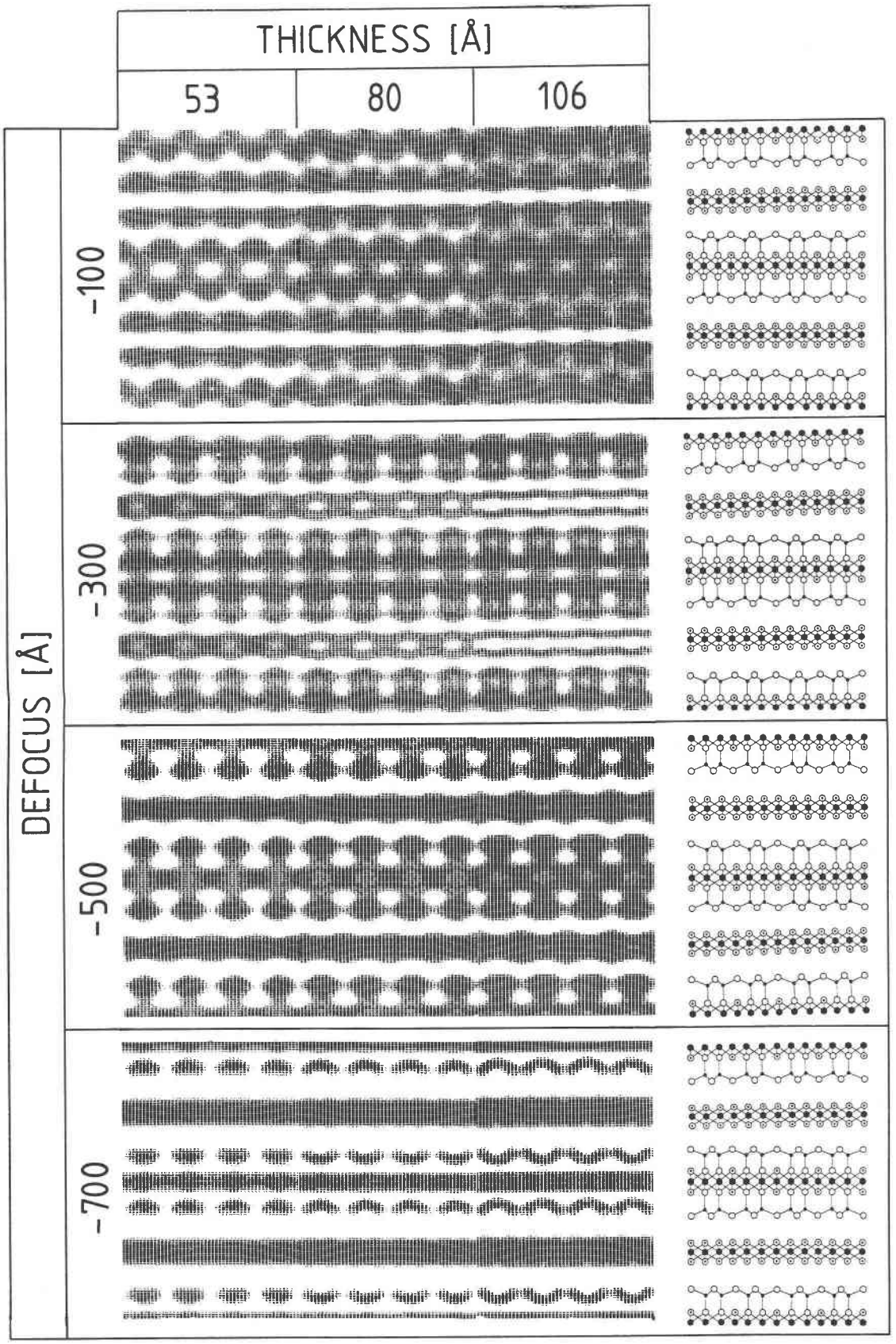
THICKNESS [Å]
53
80
106
DEFOCUS [Å]
-100
-300
-500
-700

divergence, defocus value), but other parameters such as crystal structure and sample thickness will be unknown. In practice a set of images is calculated for a range of realistic defocus values and specimen thicknesses, and this set is compared with the corresponding experimental images (e.g., Self et al., 1985). The images shown in Figures 4 and 5 have been calculated using the multislice approach (Goodman and Moodie, 1974). These calculations have been repeated using the real-space method (Van Dyck and Coene, 1984; Coene and Van Dyck, 1984a, 1984b), yielding similar images.

Figure 4 shows a set of calculated images for monoclinic chlorite, viewed along the [100] direction, for varying defocus and specimen thickness. It is clear that the image does not vary strongly with specimen thickness over the range considered here. Also, the images taken at a defocus near −500 Å are easily interpreted in terms of the crystal structure. The octahedral sheets (both the one in the 2:1 layer and that in the octahedral brucite sheet) are represented by continuous dark bands; the tetrahedra, which are grouped in columns in this projection (see Fig. 2c) are visible as dark "blobs" at both sides of the octahedral sheet of the 2:1 layer. In the ordered structure presented here, the tetrahedral columns are exactly opposite each other, both across the 2:1 layer and across the brucite interlayer. Figure 5 shows some images calculated for varying crystal structures at a defocus of −500 Å. It is clear that images taken along the ⟨100⟩ directions are easy to interpret, as the octahedral sheets are visible as dark bands, and the tetrahedral columns form dark "blobs" attached to the octahedral sheet. Such a simple relationship between crystal structure and image is often referred to as an *imaging code,* by which many defects in the perfect structure can be readily interpreted (Van Dyck et al., 1982). Shifts between adjacent layers can then be detected as shifts between the dark "blobs" representing the tetrahedral columns. Deviating structures, such as the 1:1 phyllosilicate structure, are also recognizable as a deviating distribution of octahedral and tetrahedral sheets.

Experimental images: Results and discussion

Four distinctive cases have been investigated with HRTEM: (1) relatively well ordered chlorite, (2) chlorite with a semirandom stacking, (3) chlorite showing isolated 9-Å fringes, and (4) chlorite with 7-Å fringes. All images are taken along the ⟨100⟩ direction. The defocus value is close to −500 Å, as indicated by analysis of the images of the amorphous areas at the edge of the thin foil (Spence, 1981). The results of the four cases will be discussed below.

Relatively well ordered chlorite

The diffraction pattern shown in Figure 6a has well-defined spots and only minor streaking of rows with $k \neq 3n$. These features indicate that the crystal has a relatively well ordered stacking sequence. Figure 6b shows a HRTEM image of the same crystal; the calculated image for the appropriate imaging conditions is also given. There is good agreement between the experimental image and the calculated image. Also, the variation of the image with specimen thickness agrees well with the calculated images in Figure 4. This agreement allows an interpretation of the image in terms of the crystal structure: the 2:1 layer and the brucite interlayer are easily recognizable, as are the tetrahedral columns.

Figure 6c shows the same image at a lower magnification. In a perfectly ordered crystal the tetrahedral columns should all be aligned. This is not the case here: the tetrahedral columns across the 2:1 layer are always opposite each other, but occasional shifts across the brucite interlayer do occur.

Semirandom stacking

Figure 7a shows a diffraction pattern with sharp $k = 3n$ reflections and streaking of $k \neq 3n$ reflections, indicating a semirandom stacking sequence. The HRTEM image of this area reveals that the tetrahedral columns are not opposite each other anymore, but that shifts parallel to the basal planes occur both at the brucite interlayer and at the 2:1 layer. There is a good correspondence between the experimental image and calculated images for a chlorite structure with shifts of $b/3$ along the octahedral sheet of the 2:1 layer. There is no regular repeat sequence of these shifts, so the structure cannot be described as a polytype or a superstructure, but it is truly semirandom.

Spinnler et al. (1984) have used HRTEM to study the stacking disorder in a clinochlore chlorite crystal. X-ray observations had shown that the crystal was predominantly of the monoclinic II*b*-2 polytype. The semirandom stacking sequence of their crystal is reflected in electron-diffraction patterns by streaking of rows with $k \neq 3n$. However, the streaking is not complete, and weak maxima occur along the streaks, showing that most of the crystal is monoclinic (Spinnler et al., 1984). Thus Spinnler et al. (1984) were able to describe the stacking disorder in terms of shifts relative to the ordered IIb-2 polytype and therefore as intercalations of different polytypes.

In the case of the disordered chlorite crystals of the present study, the streaking of the rows with $k \neq 3n$ in electron-diffraction patterns is complete in most cases (e.g.,

←

Fig. 4. Calculated HRTEM images of monoclinic chlorite projected along [100] for varying defocus value and specimen thickness. The images have been calculated using the multislice method. The composition is derived from electron-microprobe analyses (see text). The atom positions and Debeye-Waller factors are derived from Bailey (1975) and Shirozu and Bailey (1965). The instrumental parameters are accelerating voltage 200 kV, spherical aberration $C_s = 1.2$ mm, beam divergence 10^{-3} rad, focus spread 50 Å.

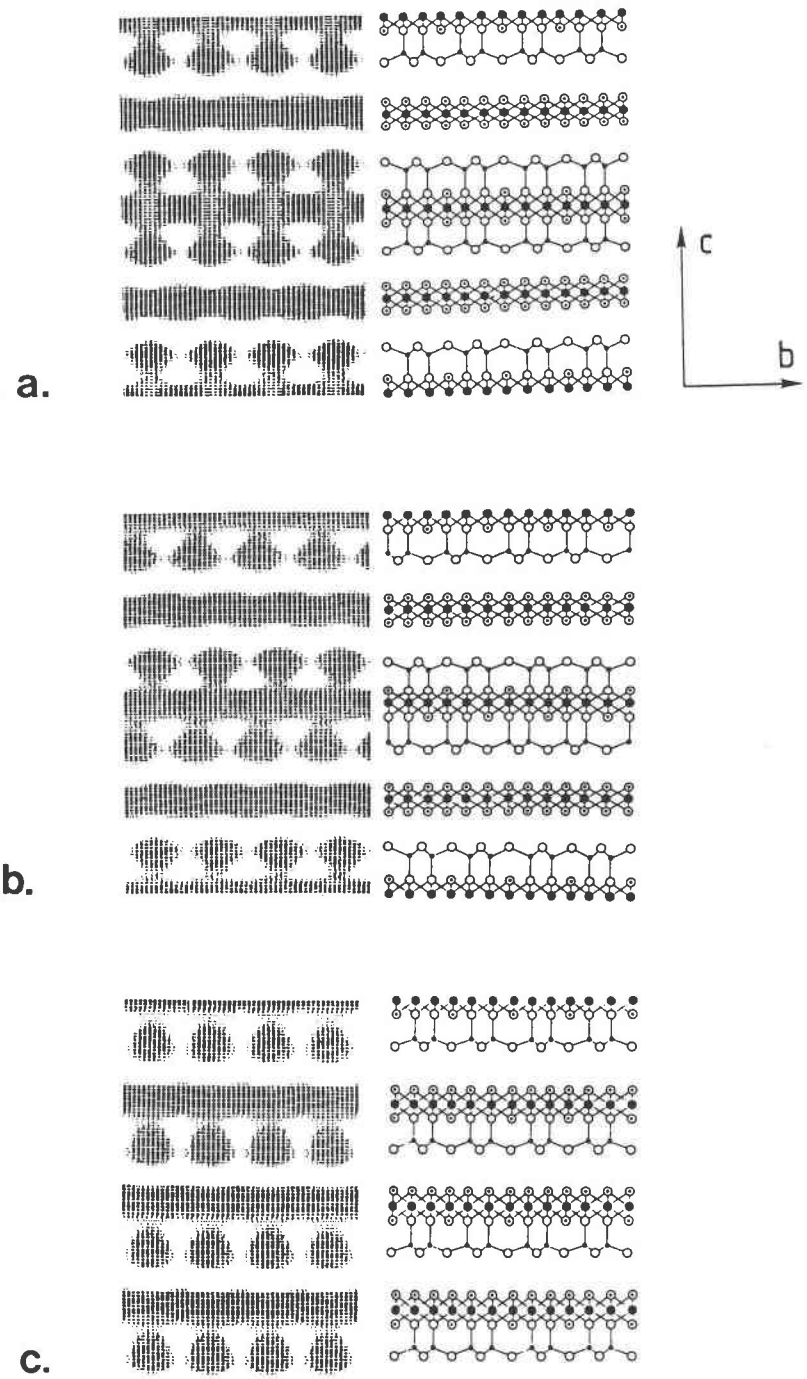

Fig. 5. Calculated HRTEM images of monoclinic chlorite and deviating structures. Specimen thickness 53 Å, defocus value −500 Å, other parameters as in Fig. 4. (**a**) Ordered chlorite. (**b**) Chlorite with shifts of $b/3$ parallel to the sheets. (**c**) 1:1 phyllosilicate with the same composition as the chlorites in the previous calculations.

→

Fig. 6. Relatively well ordered chlorite, viewed along a ⟨100⟩ direction. (**a**) Diffraction pattern showing sharp spots and only minor streaking of rows with $k \neq 3n$. The white circle indicates the objective aperture used to produce the HRTEM images. (**b**) HRTEM image taken at a defocus of ca. −500 Å. The inset is a calculated image. Specimen thickness increases from top to bottom. There is good agreement between experimental and calculated image, allowing an interpretation of the experimental image in terms of the tetrahedral (T) and octahedral (O) sheets and the brucite (B) interlayer. (**c**) The same image as in (b) at a lower magnification. Opposite tetrahedral columns are connected with white arrows. No shifts occur across the 2:1 layers, and only occasionally a shift occurs across a brucite interlayer.

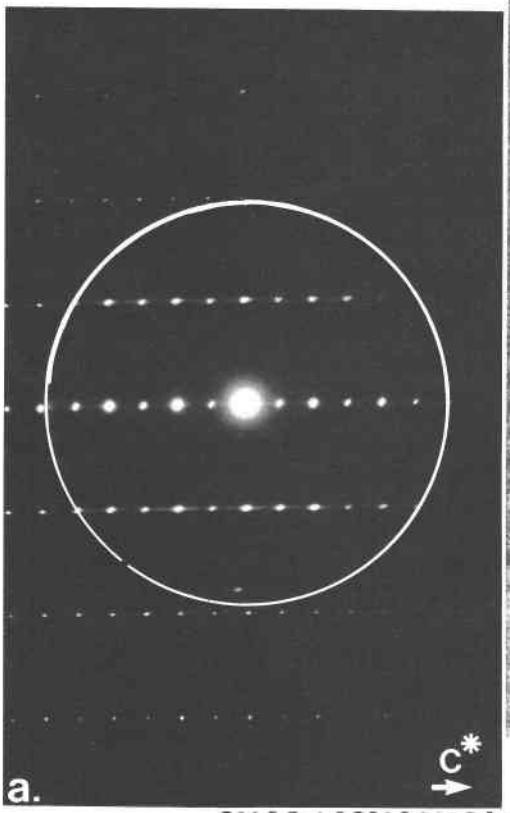
a.
c*

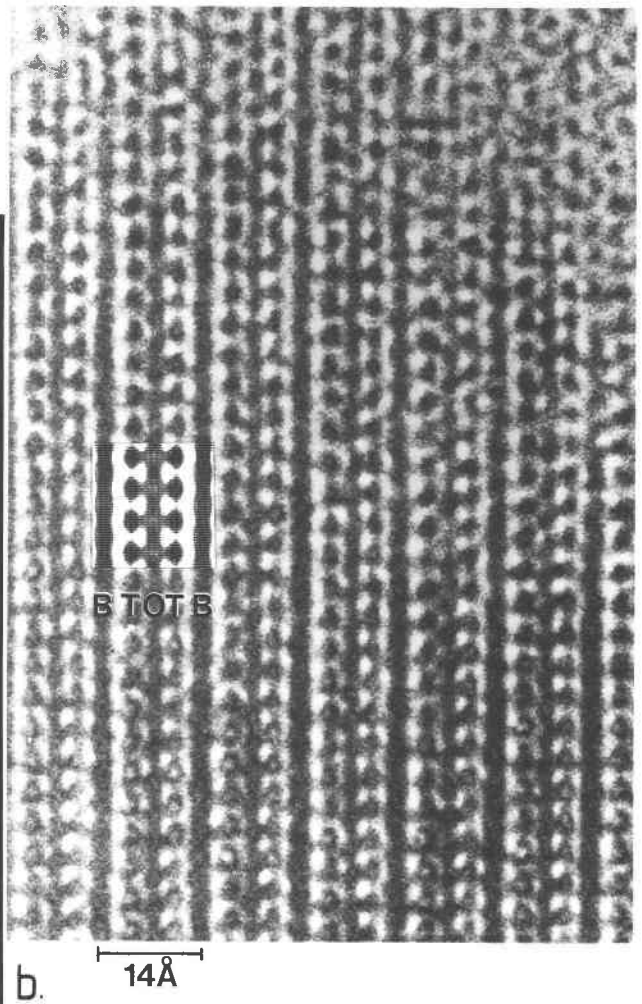
B TOT B
14Å
b.

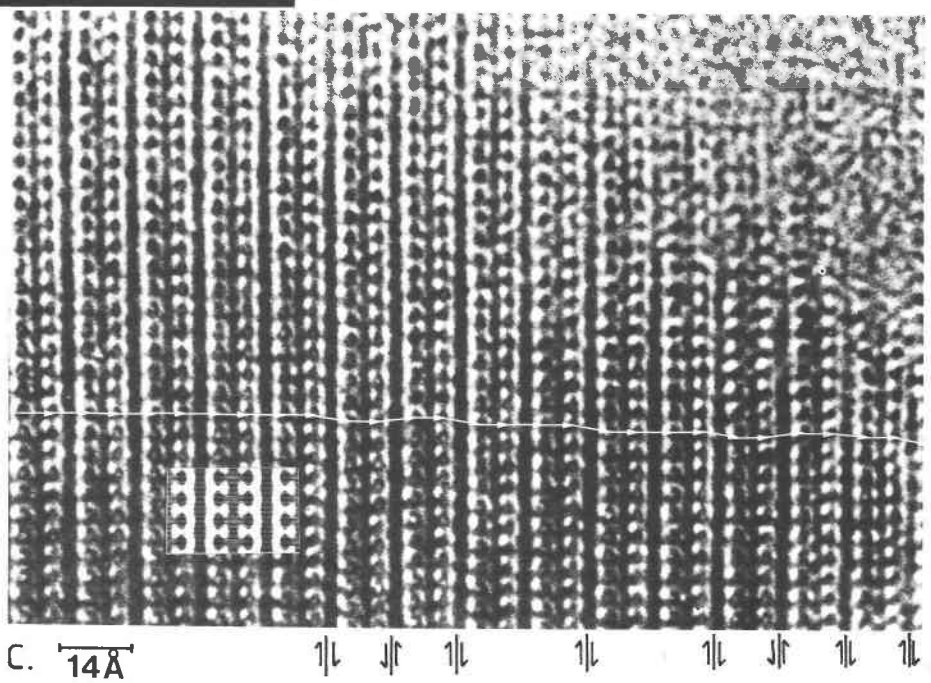
C. 14Å

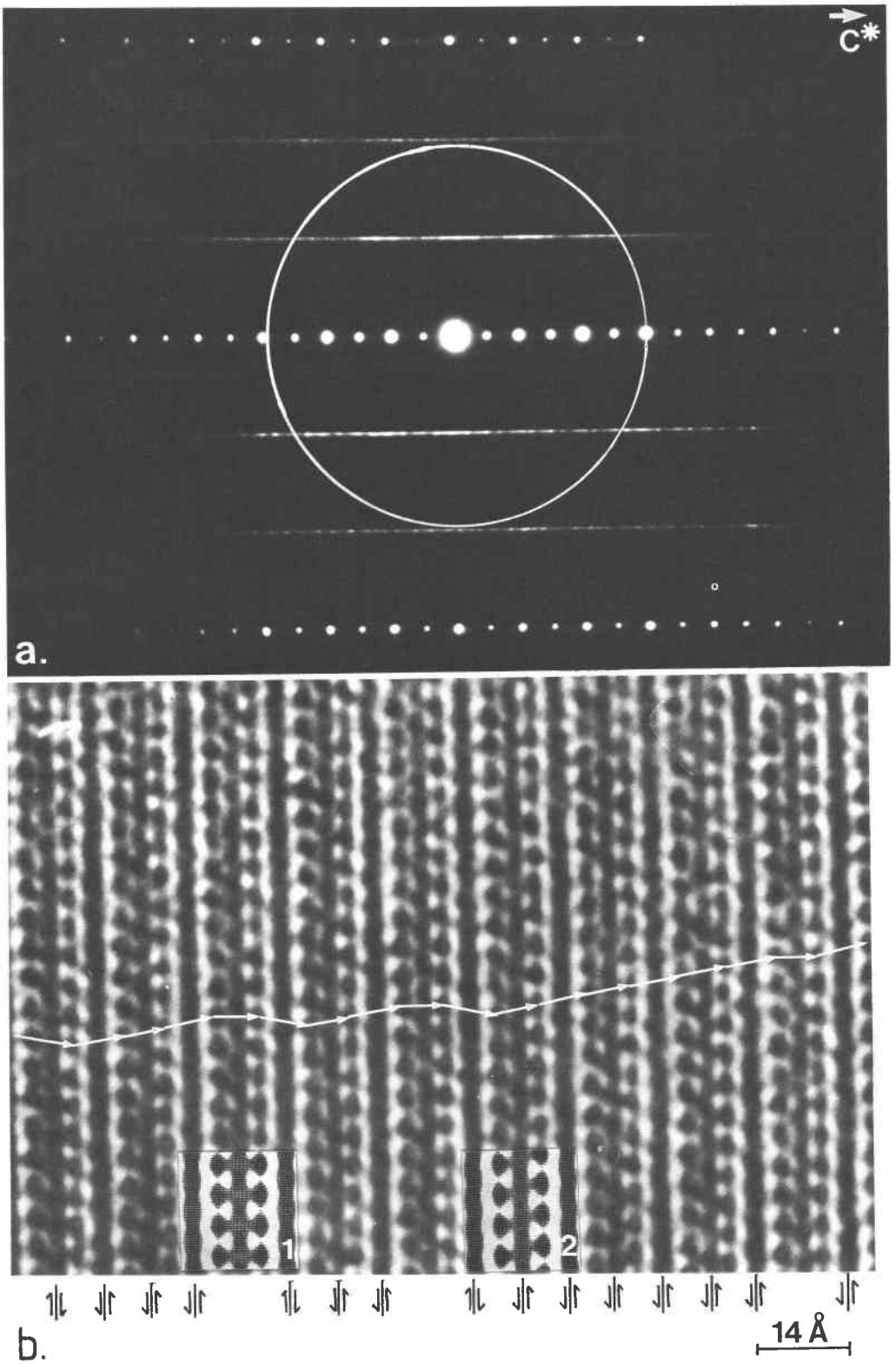

Fig. 7. Chlorite with a semirandom stacking sequence, imaged under the same conditions as in Fig. 6. (**a**) Diffraction pattern showing complete streaking of rows with $k \neq 3n$. The white circle indicates the objective aperture used to produce the HRTEM image. (**b**) Experimental HRTEM image. As in Fig. 6 the white arrows connect opposite tetrahedral columns; shifts occur both at the brucite interlayer and across the 2:1 layer. The insets are calculated images: (**1**) undisturbed chlorite crystal, (**2**) shift of $b/3$ across the 2:1 layer.

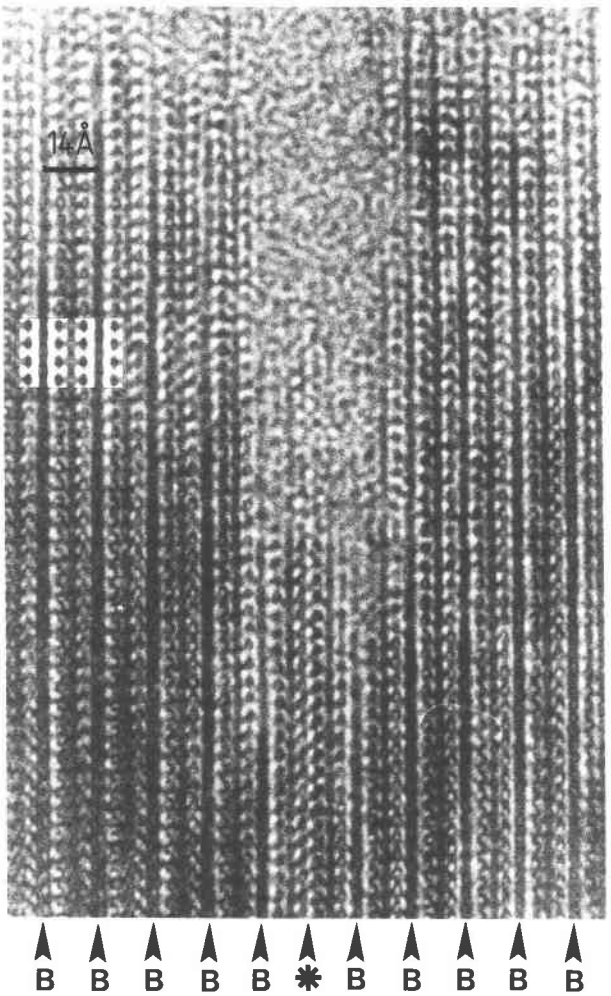

Fig. 8. HRTEM image of an area where a 9-Å lattice fringe is intercalated between 14-Å chlorite (001) fringes. The inset shows a calculated image for the chlorite structure. At the bottom, the brucite interlayers are marked with B. At the asterisk, one brucite interlayer is missing.

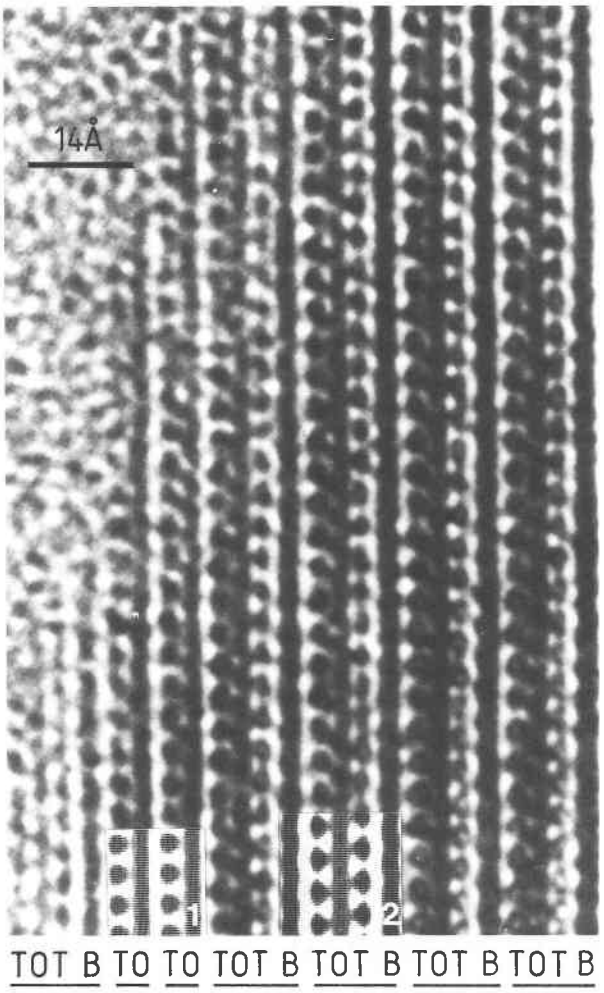

Fig. 9. HRTEM image of an area with 7-Å lattice fringes. The inset shows calculated images for a 1:1 phyllosilicate (**1**) and chlorite (**2**). T = tetrahedral sheet, O = octahedral sheet, B = brucite interlayer. The 7-Å fringes are caused by intercalations of a 1:1 phyllosilicate structure.

Fig. 7a), and it is not possible to determine the space group of the crystals. Therefore even the diffraction pattern of the relatively well ordered crystal of Figure 6 cannot be interpreted unambiguously: the 90° angle between $00l$ and $hk0$ can indicate either the [100] zone of a monoclinic crystal or one of the ⟨100⟩ directions of an orthohexagonal crystal. An interpretation of the HRTEM images in terms of one-layer polytypes is therefore not possible. Nevertheless, the HRTEM images clearly show that the semirandom stacking is caused by shifts in the (001) planes that can occur either at the brucite interlayer or in the 2:1 layer.

The frequent occurrence of shifts of magnitude $b/3$ in the ⟨010⟩ directions suggests that such deviations from the ordered stacking sequence do not significantly increase the energy of the crystal. Consequently, deformation-induced stacking faults with similar displacement vectors will have a very low stacking-fault energy. The low stacking-fault energy can explain the wide dissociation of dislocations with Burgers vectors of the form ⟨010⟩, as observed by Bons (1988a). Also, the fringe contrast of such deformation-induced stacking faults, when inclined to the electron beam, will be obscured by the fringe contrast caused by the stacking disorder, thus hampering the observation of the deformation-induced defects. This is discussed in more detail by Bons (1988a).

Chlorite with 9-Å fringes

A HRTEM image of an area where a single 9-Å fringe is intercalated between 14-Å fringes is given in Figure 8. The crystal structure of chlorite is easily recognized at the left- and right-hand sides of the micrograph. At the position of the 9-Å fringe, the brucite interlayer is missing. Thus, locally the chlorite structure is disturbed, and one can speak of a single layer with a talc structure.

Chlorite with 7-Å fringes

Figure 9 shows a HRTEM image of an area with 7-Å fringes. Again, the chlorite structure can be recognized in the undisturbed part of the crystal. The image structure at the position of the 7-Å fringes is characterized by two dark bands, each with a series of "blobs" at one side, suggesting a structure formed by a single tetrahedral sheet attached to a single octahedral sheet, i.e., a 1:1 phyllosilicate. To check whether this interpretation is valid, the experimental image is compared with a calculated image for a 1:1 phyllosilicate. There is good agreement between experimental and calculated images, and therefore these 7-Å fringes are interpreted as intercalations of a 1:1 phyllosilicate.

The last two examples show that in the chlorites studied here, the deviating lattice fringe spacings observed in a conventional transmission electron microscope are actually caused by intercalations with a different crystal structure, resulting in local deviations of the lattice spacing; they are clearly different from the deformation-induced stacking faults (see Bons, 1988a).

The observations mentioned above clearly demonstrate that HRTEM is a very powerful tool in the study of crystal imperfections, especially in cases where conventional TEM cannot resolve the nature of those imperfections.

Conclusions

Several types of stacking irregularities in chlorite crystals from slates of the Seo Formation, Orri dome, central Pyrenees, Spain, have been studied with HRTEM. The semirandom stacking is caused by shifts parallel to the basal planes, which occur at the level of the brucite interlayer as well as in the 2:1 layer. There is no regular repeat sequence of these shifts in the direction of the c-axis.

Deviations of the normal lattice-fringe spacing of 14 Å are caused by actual deviations of the crystal-lattice spacing. The 9-Å fringes are associated with a missing brucite interlayer, i.e., an intercalation of a single layer with a talc structure. The 7-Å fringes can be explained by intercalations of a 1:1 phyllosilicate.

In studies of deformation-induced defects in these minerals, it is important to realize that predeformation or postdeformation planar defects in the form of intercalations of another structure (talc, 1:1 phyllosilicate) can also be present. The low stacking-fault energy associated with displacements of magnitude $b/3$ in the $\langle 010 \rangle$ directions can explain the wide dissociation of dislocations in chlorites.

Acknowledgments

We wish to thank Professor J. van Landuyt of the University of Antwerp (R.U.C.A.) for providing the HRTEM facilities. C. F. Woensdregt and W. Coene are thanked for their assistance with the image calculations. We are grateful to S. W. Bailey, G. E. Spinnler, C. F. Woensdregt, R. O. Felius, and M. R. Drury for their comments on the manuscript. The JEOL JEM-200C electron microscope at the University of Utrecht is financed by the Dutch Organization for the Advancement of Pure Research (N.W.O.) and by the Department of Geology of the University of Utrecht.

References cited

Ahn, J.H., and Peacor, D.R. (1985) Transmission electron microscopic study of diagenetic chlorite in Gulf Coast argillaceous sediments. Clays and Clay Minerals, 33, 228–236.

Amelinckx, S., and Van Landuyt, J. (1976) Vlakke kristaldefekten, niet-stoichiometrie en polytypie. Chemisch Weekblad, 1976, m313–m320.

Amouric, M., Gianetto, I., and Proust, D. (1988) 7, 10 and 14 Å mixed-layer phyllosilicates studied structurally by TEM in pelitic rocks of the Piemontese zone (Venezuela). Bulletin Minéralogique, 111, 29–37.

Bailey, S.W. (1975) Chlorites. In J.E. Gieseking, Ed., Soil components, vol. II: Inorganic components, p. 191–263. Springer-Verlag, New York.

——— (1980a) Summary of recommendations of AIPEA nomenclature committee on clay minerals. American Mineralogist, 65, 1–7.

——— (1980b) Structures of layer silicates. In G. W. Brindley and G. Brown, Eds., Crystal structures of clay minerals and their X-ray identification, p. 1–124. Mineralogical Society Monograph no. 5, London.

——— (1988) Chlorites: Structures and crystal chemistry. In S. W. Bailey, Ed., Hydrous phyllosilicates (exclusive of micas). Mineralogical Society of America Reviews in Mineralogy, 19, 347–404.

Bons, A.J. (1988a) Deformation of chlorite in naturally deformed low-grade rocks. Tectonophysics, 154, 149–165.

——— (1988b) Intracrystalline deformation and slaty cleavage development in very low-grade slates from the Orri Dome, Central Pyrenees. Geological Ultraiectina, 56, 173 p.

Brindley, G.W. (1980) Order-disorder in clay mineral structures. In G. W. Brindley and G. Brown, Eds., Crystal structures of clay minerals and their X-ray identification, p. 125–195. Mineralogical Society Monograph no. 5, London.

Brown, B.E., and Bailey, S.W. (1962) Chlorite polytypism: I. Regular and semi-random one-layer structures. American Mineralogist, 47, 819–850.

Coene, W., and Van Dyck, D. (1984a) The Real Space Method for dynamical electron diffraction calculations in high resolution electron microscopy. II. Critical analysis of the dependency on input parameters. Ultramicroscopy, 15, 41–50.

——— (1984b) The Real Space Method for dynamical electron diffraction calculations in high resolution electron microscopy. III. A computational algorithm for the electron propagation with its practical applications. Ultramicroscopy, 15, 287–300.

Edington, J.W. (1975) Interpretation of transmission electron micrographs. Monographs in Practical Electron Microscopy in Materials Science No. 3, 112 p. Philips Technical Library–MacMillan, London.

Goodman, P., and Moodie, A.F. (1974) Numerical evaluation of N-beam wave functions in electron scattering by the multislice method. Acta Crystallographica, A30, 280–290.

Hartevelt, J.J.A. (1970) Geology of the Upper Segre and Valira Valleys, Central Pyrenees, Andorra/Spain. Leidse Geologische Mededelingen, 45, 167–236.

Jahren, J. (1988) High resolution imaging of chlorites and illites. A comparative study of calculated and experimental images. Ultramicroscopy, 24, 70.

Lee, J.H., and Peacor, D.R. (1983) Intralayer transitions in phyllosilicates of Martinsburg shale. Nature, 303, 608–609.

Lee, J.H., Peacor, D.R., Lewis, D.D., and Wintsch, R.P. (1984) Chlorite–illite/muscovite interlayered and interstratified crystals: A TEM/STEM study. Contributions to Mineralogy and Petrology, 88, 372–385.

Maresh, W.V., Massone, H.J., and Czank, M. (1985) Ordered and disordered chlorite/biotite interstratifications as alteration products of chlorite. Neues Jahrbuch für Mineralogie, Abhandlungen, 152, 79–100.

Olives, J. (1985) Biotites and chlorites as interlayered biotite-chlorite crystals. Bulletin Minéralogique, 108, 635–641.

Olives, J., and Amouric, M. (1984) Biotite chloritization by interlayer brucitization as seen by HRTEM. American Mineralogist, 69, 869–871.

Self, P.G., Glaisher, R.W., and Spargo, A.E.C. (1985) Interpreting high-resolution transmission electron micrographs. Ultramicroscopy, 18, 49–62.

Shirozu, H., and Bailey, S.W. (1965) Chlorite polytypism: III. Crystal structure of an orthohexagonal iron chlorite. American Mineralogist, 50, 868–885.

Speksnijder, A. (1987) The structural development of the Orri Dome, southern Variscan Pyrenees, Spain. Eclogae Geologicae Helvetiae, 80, 697–733.

Spence, J.C.H. (1981) Experimental high-resolution electron microscopy. Monographs on the physics and chemistry of materials, 370 p. Clarendon Press, Oxford.

Spinnler, G.E., Self, P.G., Iijima, S., and Buseck, P.R. (1984) Stacking disorder in clinochlore chlorite. American Mineralogist, 69, 256–263.

Van Dyck, D. (1986) High-resolution electron microscopy. In Microscopia elettronica in transmissione e techniche di analisi di superfici nella scienza dei materiali, parte B: Microscopia elettronica in trasmissione, p. 281–425, Edizione Enea, Roma.

Van Dyck, D., and Coene, W. (1984) The Real Space Method for dynamical electron diffraction calculations in high resolution electron microscopy. I. Principles of the method. Ultramicroscopy, 15, 29–40.

Van Dyck, D., Van Tendeloo, G., and Amelinckx, S. (1982) Direct interpretation of high resolution electron images of substitutional alloy systems with a column structure. Ultramicroscopy, 10, 263–280.

Veblen, D.R. (1983) Microstructures and mixed layering in intergrown wonesite, chlorite, talc, biotite, and kaolinite. American Mineralogist, 68, 566–580.

Manuscript received October 10, 1988
Manuscript accepted May 8, 1989